

Algoritmos eficientes para aplicaciones en tomografía óptica

Lic. Enzo Leopoldo Gaggioli

Defensa de Tesis Doctoral

Director: Darío Mitnik

Codirector: Claudio Delrieux

En col. con Prof. Oscar P. Bruno, Caltech

Departamento de Física
Facultad de Ciencias Exactas y Naturales
Universidad de Buenos Aires



Resumen

- ▶ Introducción.
 - ▶ Problema de transporte de radiación en la materia.
 - ▶ Algoritmo para el problema *directo*.
 - ▶ Resultados de validación.
 - ▶ Capas límite.
 - ▶ Problema *inverso*.
 - ▶ Reconstrucciones tomográficas.

Publicaciones asociadas

Journal of Quantitative Spectroscopy & Radiative Transfer 236 (2019) 106589



Contents lists available at ScienceDirect

Journal of Quantitative Spectroscopy & Radiative Transfer

journal homepage: www.elsevier.com/locate/ijgsrt



Light transport with the equation of radiative transfer: The Fourier Continuation – Discrete Ordinates (FC-DOM) Method



E.L. Gaggioli ^{a,b,*}, O.P. Bruno ^c, D.M. Mitnik ^{a,b}

⁴ Instituto de Astronomía y Física del Espacio (IAFE, CONICET-UBA), Casilla de Correo 67 - Suc. 28 Buenos Aires, (C1428ZAA), Argentina

^b ECEvN, Universidad de Buenos Aires, Argentina.

^c Computing and Mathematical Sciences, Caltech, Pasadena, CA 91125, USA

ARTICLE INFO

Article history:

Received 14 March 2019

Revised 1 July 2019

Accepted 27 July 2019

Available online 28 July 2019

ABSTRACT

We present a method for the treatment of the time dependent radiative transfer equation under the discrete ordinate approximation. The novelty of the proposed approach stems, in part, from the incorporation of a spectral method for the calculation of the spatial differential operators based on the Fourier Continuation procedure introduced recently by Bruno and co-authors. This is a spatially dispersionless and high order method, which can handle arbitrary geometries, including those encountered in the forward model of light transport in optical tomography. We validate our theoretical results by comparison with analytic and experimental outcomes of the fluence measurements on tissue-like phantoms. The method makes it possible to calculate the time of flight of photons in random media efficiently and with high accuracy.

© 2019 Elsevier Ltd. All rights reserved.

1. Introduction

short amount of time. With this goal in mind, we have developed the present method.

Publicaciones asociadas

PHYSICAL REVIEW E 104, L032801 (2021)

Letter

Skin effect in neutron transport theory

E. L. Gaggioli^a* and D. M. Mitnik^b

Instituto de Astronomía y Física del Espacio (IAFE, CONICET-UBA), Casilla de Correo 67 - Suc. 28 (C1428ZAA), Buenos Aires, Argentina

O. P. Bruno

Computing and Mathematical Sciences, California Institute of Technology, Pasadena, California 91125, USA



(Received 25 February 2021; accepted 1 September 2021; published 20 September 2021)

We identify a neutron-flux “skin effect” in the context of neutron transport theory. The skin effect, which emerges as a boundary layer at material interfaces, plays a critical role in a correct description of transport phenomena. A correct accounting of the boundary-layer structure helps bypass computational difficulties reported in the literature over the last several decades, and should lead to efficient numerical methods for neutron transport in two and three dimensions.

DOI: 10.1103/PhysRevE.104.L032801

The physical character of the neutron fluxes within and around heterogeneous materials, for given sources, has been the subject of significant literature over the last 70 years [1–7]. Much of this literature has been devoted to unraveling the complex interactions that result from the combined effect of neutron collision and transport phenomena [2–5]. This Letter describes and analyzes a physical observable, namely, a neutron-flux “skin effect” near physical boundaries, wherein sizable neutron fluxes exist for *incoming directions* nearly parallel to the boundary even in cases in which the exterior region is a source-free vacuum. The skin effect impacts in

A mathematical reformulation of the neutron transport problem via a combination of changes of variables for the spatial and angular variables is presented in this Letter, which facilitates the skin-effect analysis. In particular, this approach enables the accurate modeling of neutron fluxes at arbitrarily small distances from the domain boundary, and, therefore, everywhere in the combined angular-spatial domain.

The equation for time-independent neutron transport in a one-dimensional plane-parallel geometry (Fig. 1), with isotropic scattering and vacuum boundary conditions, is given by [9,11]

Publicaciones asociadas

Journal of Quantitative Spectroscopy & Radiative Transfer 290 (2022) 108300



Contents lists available at ScienceDirect

Journal of Quantitative Spectroscopy & Radiative Transfer

journal homepage: www.elsevier.com/locate/jqsrt



Parallel inverse-problem solver for time-domain optical tomography with perfect parallel scaling



E.L. Gaggioli^{a,b}, Oscar P. Bruno^{c,*}

^a Instituto de Astronomía y Física del Espacio (IAFE, CONICET-UBA), Casilla de Correo 67 - Suc. 28 (C1428ZAA), Buenos Aires, Argentina.

^b Departamento de Física, FCEyN, Universidad de Buenos Aires, Argentina.

^cComputing and Mathematical Sciences, Caltech, Pasadena, CA 91125, USA

ARTICLE INFO

Article history:

Received 17 February 2022

Revised 30 May 2022

Accepted 21 June 2022

Available online 24 June 2022

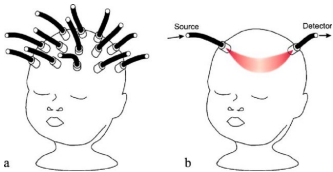
ABSTRACT

This paper presents an efficient *parallel* radiative transfer-based inverse-problem solver for time-domain optical tomography. The radiative transfer equation provides a physically accurate model for the transport of photons in biological tissue, but the high computational cost associated with its solution has hindered its use in time-domain optical-tomography and other areas. In this paper this problem is tackled by means of a number of computational and modeling innovations, including (1) A spatial parallel-decomposition strategy with *perfect parallel scaling* for the forward and inverse problems of optical tomography on parallel computer systems; and, (2) A Multiple Staggered Source method (MSS) that solves the inverse transport problem at a computational cost that is *independent of the number of sources employed*, and which significantly accelerates the reconstruction of the optical parameters; a six-fold MSS acceleration factor is demonstrated in this paper. Finally, this contribution presents (3) An intuitive derivation of the adjoint-based formulation for evaluation of functional gradients, including the highly-relevant general Fresnel boundary conditions—thus, in particular, generalizing results previously available for vacuum boundary conditions. Solutions of large and realistic 2D inverse problems are presented in this paper, which were produced on a 256-core computer system. The combined parallel/MSS acceleration approach reduced the required computing times by several orders of magnitude, from months to a few hours.

Motivación

- ▶ La Ecuación de Transporte Radiativo (ETR) modela el transporte de partículas neutras.
- ▶ Aplicaciones:
 - Radiación térmica.
 - Dinámica de gases.
 - Atmósferas estelares y planetarias.
 - Radioterapia y fototerapia.
 - Desarrollo y diseño de reactores nucleares.
 - Diagnóstico médico: TC, PAT, tomografía óptica (DOT, fDOT).
- ▶ Requiere métodos eficientes.

Tomografía óptica



Figuras de Cooper et. al. (2017). <https://doi.org/10.1038/pr.2017.107> y Hebden et. al. (2007).
<https://doi.org/10.1007/s00330-007-0659-1>

Ventajas relativas de la tomografía óptica

- ▶ Bajo costo (PET, TC, MRI).
- ▶ Portabilidad (PET, TC, MRI).
- ▶ No invasiva y versátil.
- ▶ Radiación no ionizante. No cancerígena, a diferencia de rayos X (TC, PET).

Intensidad específica

Flujo de energía irradiada

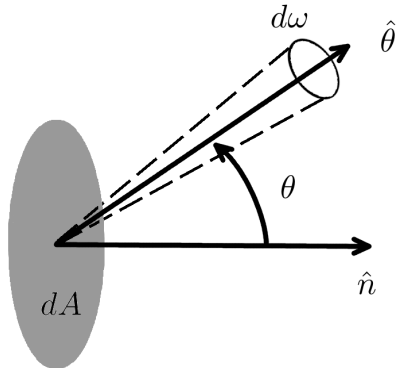
$$dE_\nu = u_\nu(x, y, z, \hat{\theta}, t) \cos(\theta) d\nu dA d\omega dt$$

$$[J] = [u_\nu][Hz][m^2][sr][s]$$

Intensidad específica de radiación: $u_\nu(x, y, z, \hat{\theta}, t)$

$$[u_\nu] = [W][m^{-2}][sr^{-1}][Hz^{-1}]$$

$$\hat{\theta} \cdot \hat{n} = \cos(\theta)$$



La Ecuación de Transferencia Radiativa

Problema ETR dependiente del tiempo:

$$\frac{1}{c} \frac{\partial u}{\partial t} + \hat{\theta} \cdot \nabla u + au + bu = b \int_{S^1} \eta(\hat{\theta} \cdot \hat{\theta}') u(\mathbf{x}, \hat{\theta}', t) d\theta' + s$$

Chandrasekhar, *Radiative Transfer*, 1950.

La Ecuación de Transferencia Radiativa

Problema ETR dependiente del tiempo:

$$\frac{1}{c} \frac{\partial u}{\partial t} + \hat{\theta} \cdot \nabla u + au + bu = b \int_{S^1} \eta(\hat{\theta} \cdot \hat{\theta}') u(\mathbf{x}, \hat{\theta}', t) d\theta' + s$$

Chandrasekhar, *Radiative Transfer*, 1950.

La Ecuación de Transferencia Radiativa

Problema ETR dependiente del tiempo:

$$\frac{1}{c} \frac{\partial u}{\partial t} + \hat{\theta} \cdot \nabla u + \textcolor{red}{au} + bu = b \int_{S^1} \eta(\hat{\theta} \cdot \hat{\theta}') u(\mathbf{x}, \hat{\theta}', t) d\theta' + s$$

Chandrasekhar, *Radiative Transfer*, 1950.

La Ecuación de Transferencia Radiativa

Problema ETR dependiente del tiempo:

$$\frac{1}{c} \frac{\partial u}{\partial t} + \hat{\theta} \cdot \nabla u + au + bu = b \int_{S^1} \eta(\hat{\theta} \cdot \hat{\theta}') u(\mathbf{x}, \hat{\theta}', t) d\theta' + s$$

Chandrasekhar, *Radiative Transfer*, 1950.

La Ecuación de Transferencia Radiativa

Problema ETR dependiente del tiempo:

$$\frac{1}{c} \frac{\partial u}{\partial t} + \hat{\theta} \cdot \nabla u + au + bu = b \int_{S^1} \eta(\hat{\theta} \cdot \hat{\theta}') u(\mathbf{x}, \hat{\theta}', t) d\theta' + s$$

Chandrasekhar, *Radiative Transfer*, 1950.

La Ecuación de Transferencia Radiativa

Problema ETR dependiente del tiempo:

$$\frac{1}{c} \frac{\partial u}{\partial t} + \hat{\theta} \cdot \nabla u + au + bu = b \int_{S^1} \eta(\hat{\theta} \cdot \hat{\theta}') u(\mathbf{x}, \hat{\theta}', t) d\theta' + s$$

Condición inicial:

$$u(\mathbf{x}, \hat{\theta}, t = 0) = 0$$

Condición de borde de Fresnel:

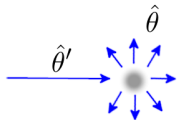
$$u(\mathbf{x}, \hat{\theta}, t) = f(\hat{n} \cdot \hat{\theta}) u(\mathbf{x}, \hat{\theta}_r, t) + q(\mathbf{x}, \hat{\theta}, t), \quad (\mathbf{x}, \hat{\theta}) \in \Gamma_-$$

Chandrasekhar, *Radiative Transfer*, 1950.

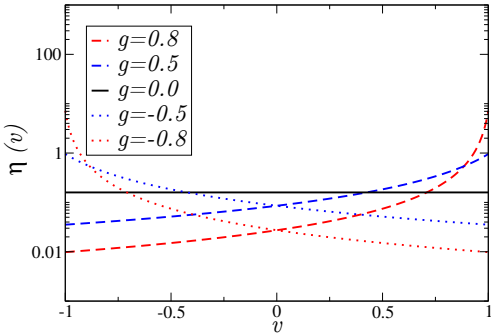
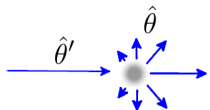
Función de fase

$$\eta(\hat{\theta} \cdot \hat{\theta}') = \frac{1}{2\pi} \frac{1 - g^2}{(1 + g^2 - 2g \hat{\theta} \cdot \hat{\theta}')^{3/2}}, \quad \int_{S^1} \eta(\hat{\theta} \cdot \hat{\theta}') d\theta' = 1.$$

$g = 0$:

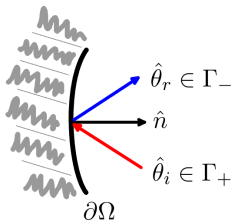


$g > 0$:

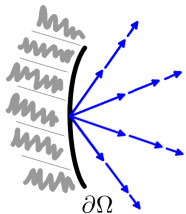


Condiciones de contorno

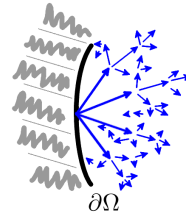
Fresnel



Régimen de transporte



Régimen difusivo

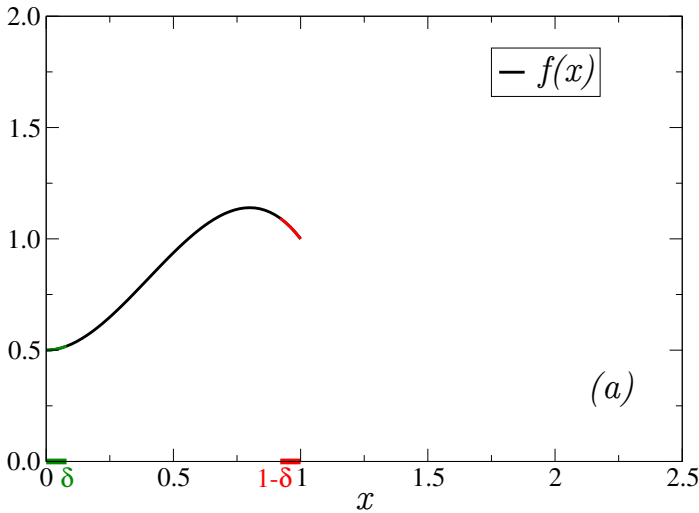


$$\Gamma_{\pm} = \{(\mathbf{x}, \hat{\theta}) \in \partial\Omega \times S^1, \pm \hat{n} \cdot \hat{\theta} < 0\}$$

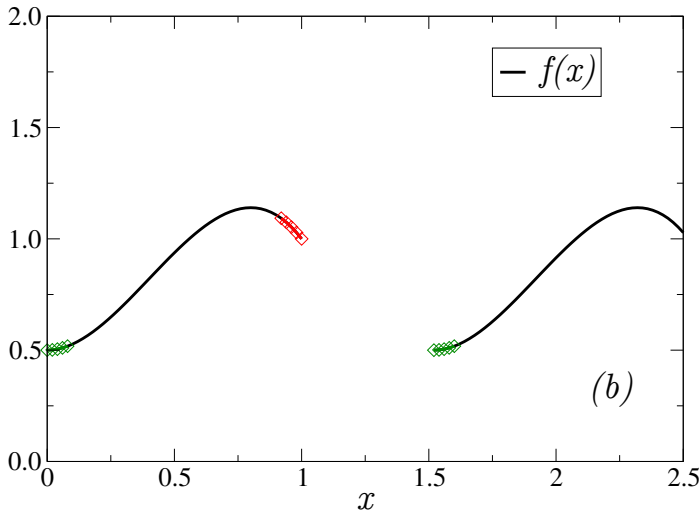
Resolución numérica: FC-DOM

- Ordenadas discretas (DOM), $\hat{\theta}_m$.
- Adams-Bashforth explícito de cuarto orden en el tiempo.
- Continuación de Fourier (FC).
- Alto orden de convergencia.

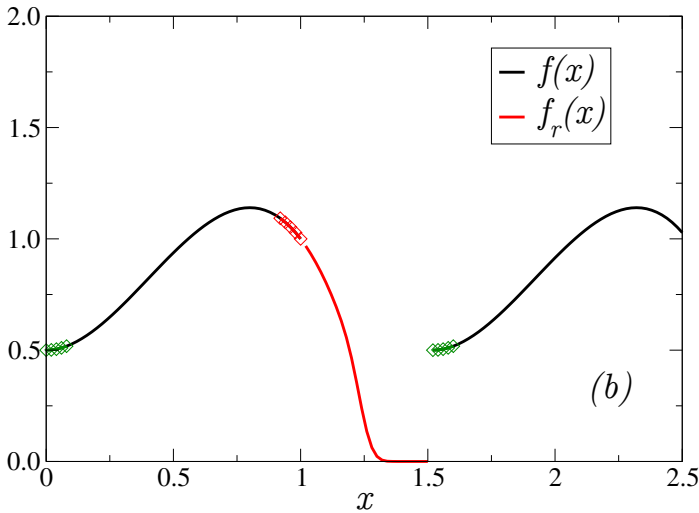
El método de continuación de Fourier



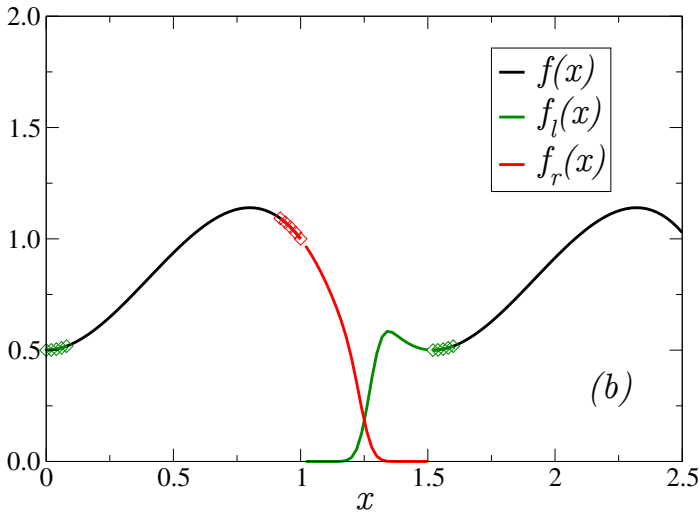
El método de continuación de Fourier



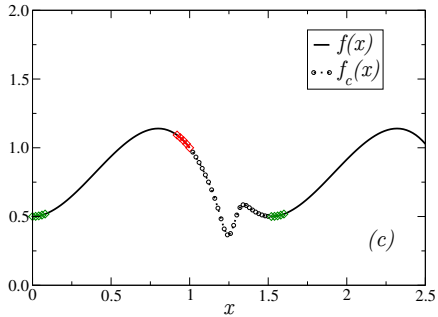
El método de continuación de Fourier



El método de continuación de Fourier



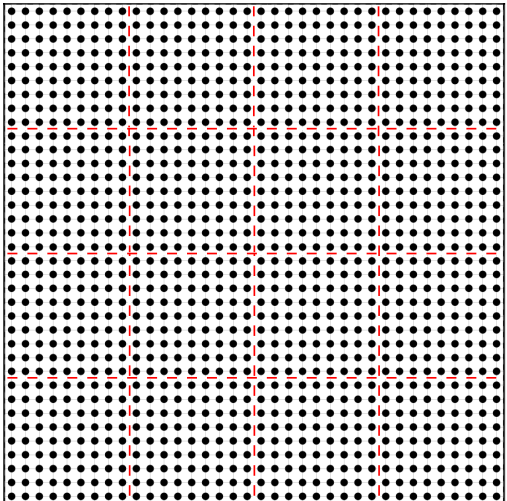
El método de continuación de Fourier



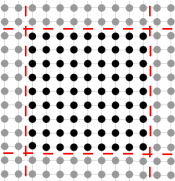
$$\frac{df}{dx}(x) \sim \frac{df_c}{dx}(x)$$

$$\frac{df_c}{dx}(x) = \sum_{k=-N_p/2}^{N_p/2} i \frac{2\pi k}{b} a_k \exp\left(i \frac{2\pi k x}{b}\right)$$

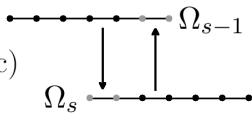
Descomposición de dominio



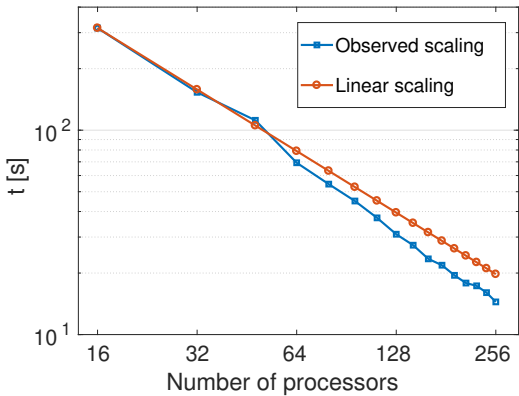
(b)



(c)



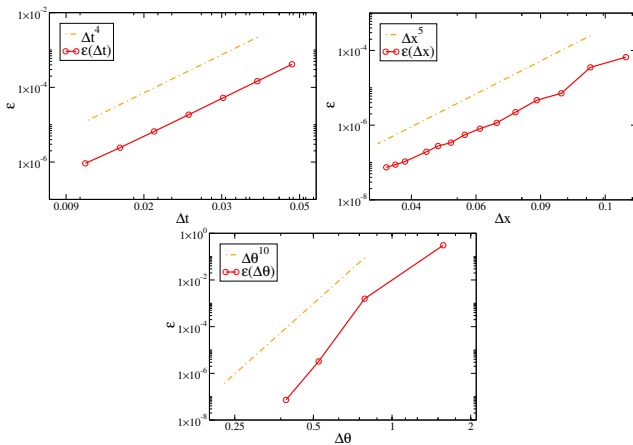
Escalabilidad



Fujii et al. (2014, JQSRT): 44 horas.
FC-DOM en 64 procesadores: < 30 minutos.

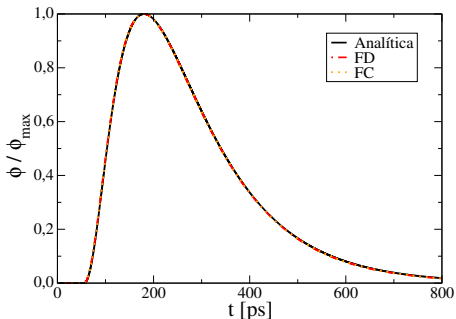
Validación: solución manufacturada

$$u^{\text{an}}(\mathbf{x}, \hat{\theta}, t) = e^{-(x-t)^2 - (y-t)^2 - \cos(\theta)^2}, \varepsilon = \max |\phi^{\text{num}} - \phi^{\text{an}}|.$$



Comparación con solución analítica

$$\phi(r,t) = \frac{e^{-ct(a+b')}}{2\pi} \delta(ct-r) + \frac{b'}{2\pi ct} \left(1 - \frac{r^2}{c^2 t^2}\right)^{-1/2} \times \exp[b' \sqrt{c^2 t^2 - r^2} - ct(a+b')] H(ct-r)$$

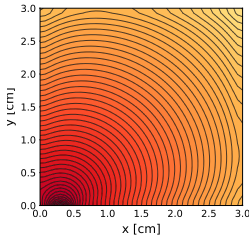
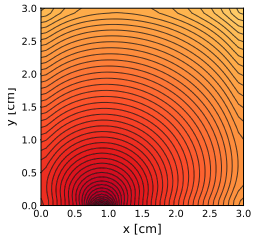
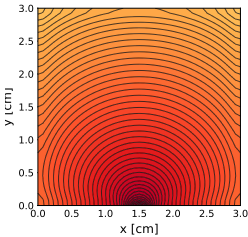
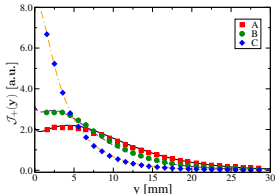
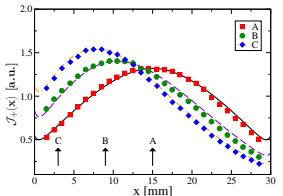
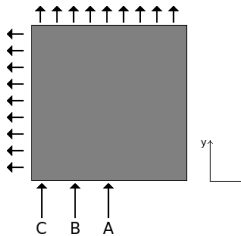


Convergencia		
Δ	FC	FD
0.250	10^{-3}	10^{-1}
0.125	10^{-4}	10^{-2}
0.100	10^{-5}	10^{-2}

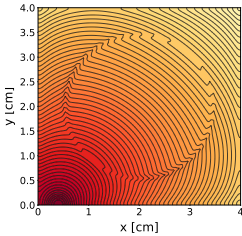
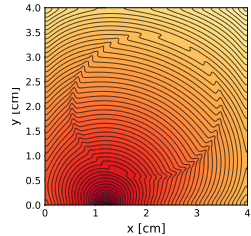
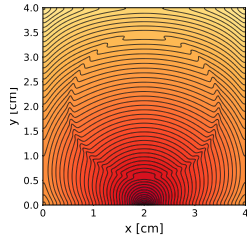
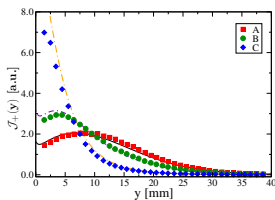
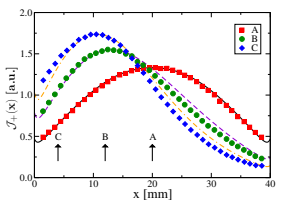
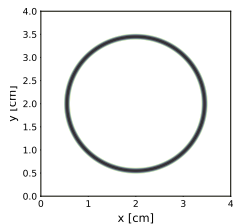
$$\Delta\phi(r) = \sqrt{\frac{\int |\phi^a - \phi^n|^2 dt}{\int |\phi^a|^2 dt}}$$

Solución analítica: Paasschens (1997).

Comparación con resultados experimentales



Comparación con resultados experimentales



Capa límite

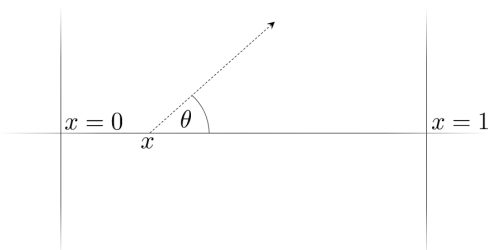
Problema 1D isótropo independiente del tiempo

$$\xi \frac{\partial}{\partial x} u(x, \xi) + \mu_t(x) u(x, \xi) = \frac{\mu_s(x)}{2} \int_{-1}^1 u(x, \xi') d\xi' + q(x, \xi)$$

Condiciones de borde de Fresnel

$$u(x = 0, \xi) = \mathcal{R}(\xi)u(x = 0, \xi_R) \quad \forall \xi > 0$$

$$u(x = 1, \xi) = \mathcal{R}(\xi)u(x = 1, \xi_R) \quad \forall \xi < 0$$



$$\xi = \cos(\theta)$$

$\xi \rightarrow 0^+$ cuando $\theta \rightarrow \pi/2$.

Capa límite

Solución interna $(x, \xi) \rightarrow (0^+, 0^+)$:

Usamos:

$$X = \frac{x}{\xi}, \quad U(X, \xi) = u(\xi X, \xi), \quad U(X, \xi) \sim U_0(X, \xi)$$

$$\frac{\partial U_0(X, \xi)}{\partial X} + \mu_t(0)U_0(X, \xi) = \frac{\mu_s(0)}{2} \int_{-1}^1 U_0\left(\frac{\xi X}{\xi'}, \xi'\right) d\xi' + q(0, \xi),$$

$$u(x, \xi) \sim u_0(x, \xi) = U_0(x/\xi, \xi)$$

Capa límite

Utilizando el factor integrante, y definiendo

$$I(x, \xi) = \int_0^x e^{\frac{\mu_t(0)y}{\xi}} \left[\frac{\mu_s(0)}{2} \int_{-1}^1 u_0(y, \xi') d\xi' + q(0, \xi) \right] dy,$$

se obtiene

$$u_0(x, \xi) = \frac{e^{-\mu_t(0)x/\xi}}{\xi} \left[\xi u(0, \xi) + I(x, \xi) \right].$$

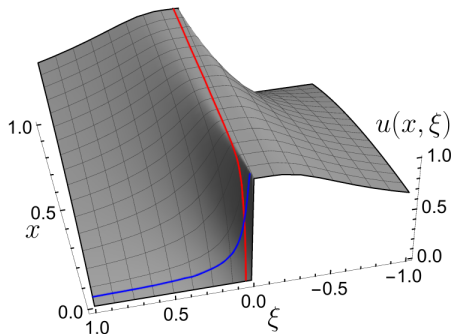
Capa límite

Estructura de capa límite con $\mu_s(x) = 0$.

$$u(x, \xi) =$$

$$\begin{cases} \frac{q}{\mu_a} \left[1 - \frac{\eta(\xi)}{e^{\mu_a x / \xi}} \right] & \forall \xi > 0, \\ \frac{q}{\mu_a} \left[1 - \frac{\eta(\xi)}{e^{\mu_a(x-1) / \xi}} \right] & \forall \xi < 0, \end{cases}$$

$$\eta(\xi) = \frac{\mathcal{R}(|\xi|) - 1}{\mathcal{R}(|\xi|) e^{-\mu_a/|\xi|} - 1}$$



$$\mathcal{R}(\xi) = 0$$

Capa límite: cambio de variable

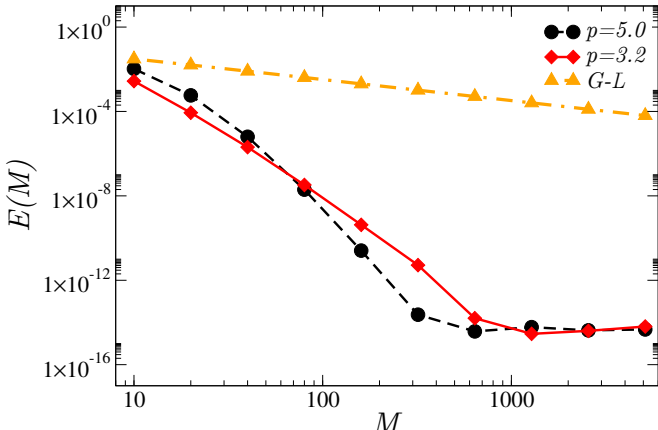
- ▶ Error de cuadratura de ℓ -puntos decrece como $32V/15\pi j(2\ell + 1 - j)^j$ siempre que la derivada j -ésima esté acotada por la constante V .
- ▶ Proponemos el cambio de variable $\xi' = r^p$.
- ▶ Buscamos una cota V para la derivada

$$\left| \frac{\partial^j}{\partial r^j} [u(x, r^p) r^{p-1}] \right| \leq W r^{p-j-1}$$

para alguna constante W .

- ▶ Llamando $V = W r^{p-j-1}$ se obtiene la cota deseada, *uniforme para todo x y r* .

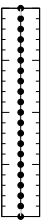
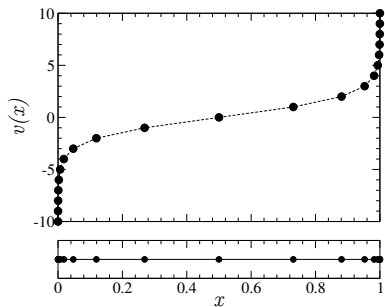
Capa límite: cambio de variable



$$E(M) = \max_x \left| \sum_{i=1}^M w_i u(x, \xi_i) - I^{\text{an}}(x) \right| \text{ con } \mathcal{R}(\xi) = 0.$$

Capa límite: cambio de variable espacial

$$v = \log\left(\frac{x}{1-x}\right)$$



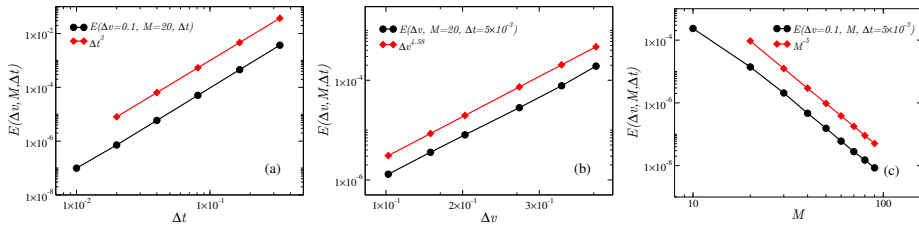
$$\begin{aligned} & \frac{\partial}{\partial t} u(v, \xi, t) + \xi(2 + 2 \cosh(v)) \frac{\partial}{\partial v} u(v, \xi, t) \\ & + \mu_t u(v, \xi, t) = \frac{\mu_s}{2} \int_{-1}^1 u(v, \xi', t) d\xi' + q, \end{aligned}$$

$$u(v, \xi, t_{\min}) = 0,$$

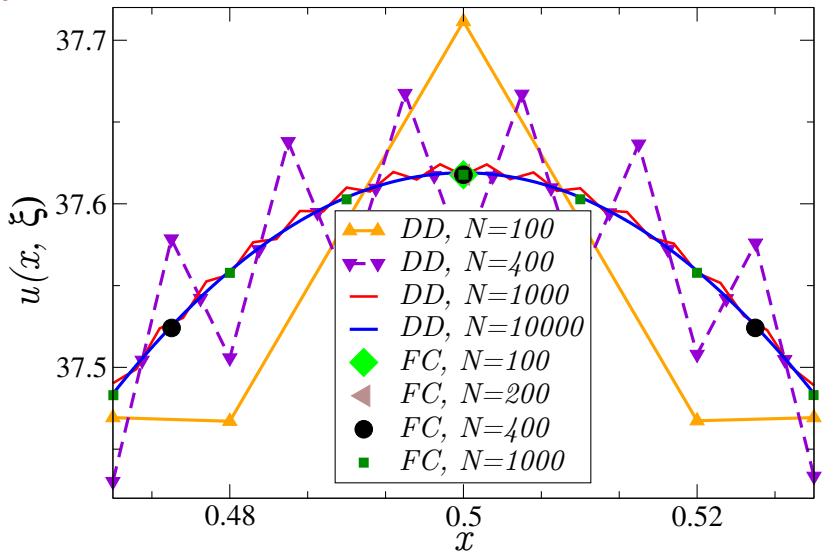
$$u(v_{\min}, \xi, t) = u_0(x'_{\min}, \xi, t) \quad \forall \xi > 0,$$

$$u(v_{\max}, \xi, t) = u_0(x'_{\max}, \xi, t) \quad \forall \xi < 0.$$

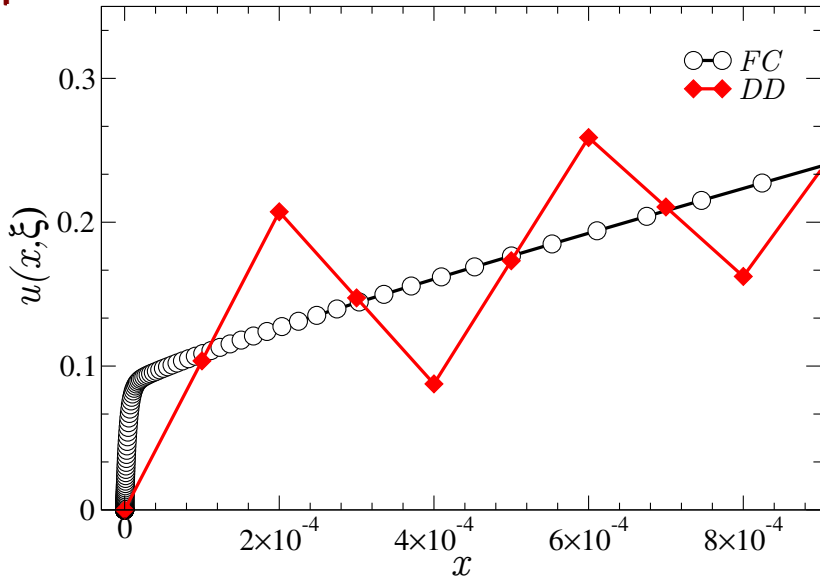
Capa límite: convergencia



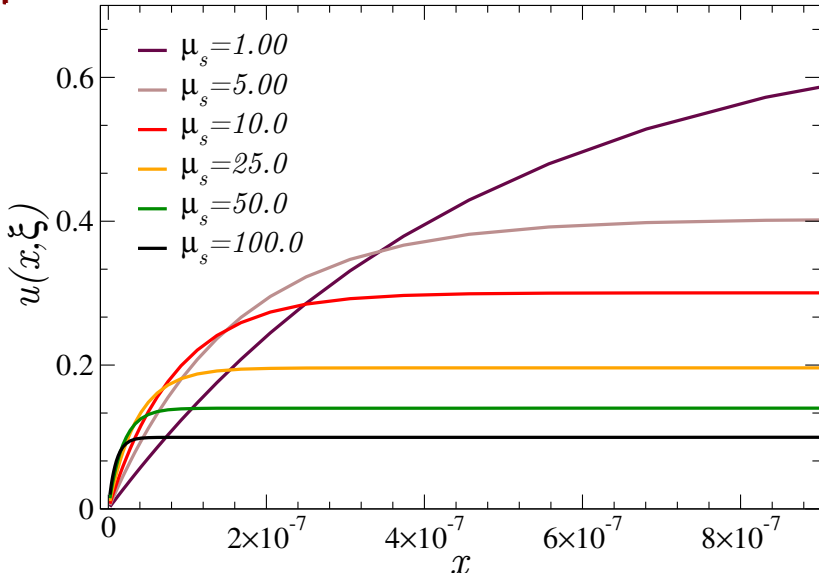
Capa límite



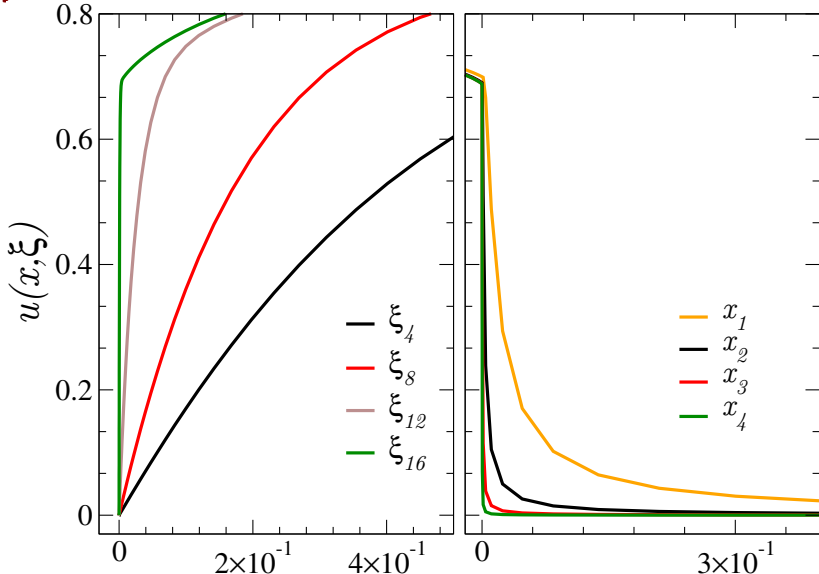
Capa límite



Capa límite



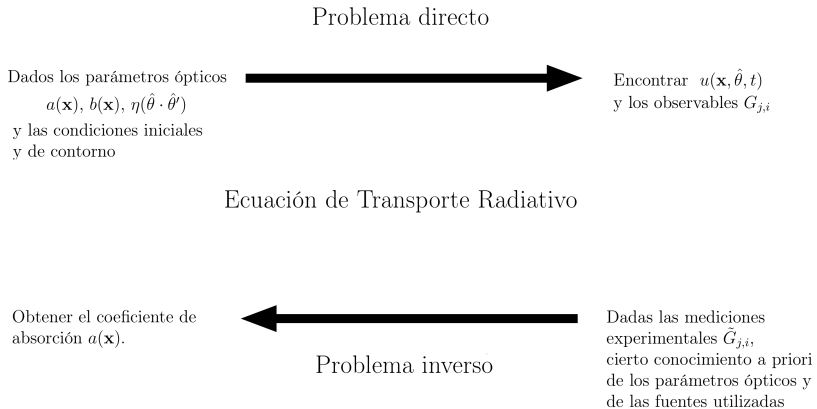
Capa límite



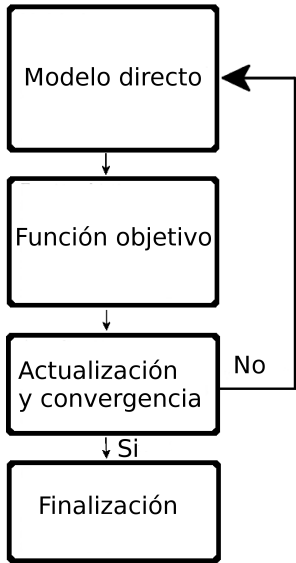
Capa límite

- Gradientes muy abruptos, que no pueden ser resueltos con los métodos estándar.
- Explicación física: valores pequeños de ξ implican caminos geométricos largos.
- Identificamos las estructuras de capas límite.
- Las resolvimos mediante cambios de variables.
- Mediante el método propuesto se logra resolver las capas límite con alto orden y de forma muy eficiente: 400 puntos en contraste a 10000 puntos requeridos por el esquema DD.

El problema inverso



Esquema MOBIIR



Método de minimización cuasi–Newton

$$\mathbf{a}^{i+1}(\mathbf{x}) = \mathbf{a}^i(\mathbf{x}) + \alpha^i \mathbf{d}^i(\mathbf{x})$$

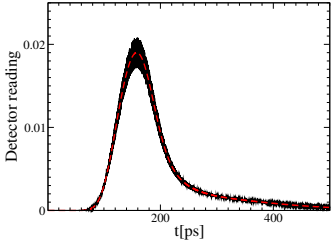
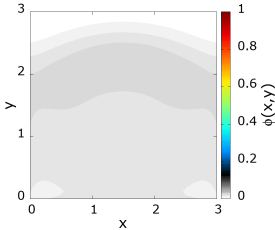
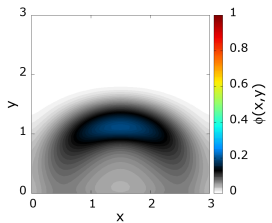
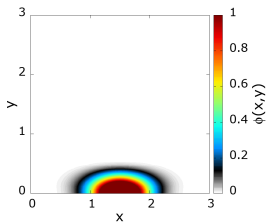
El método BFGS requiere el cálculo de $(\nabla_a^2 g^i)^{-1}$:

$$\mathbf{d}^i = -(\nabla_a^2 g^i)^{-1} \nabla_a g^i.$$

Im-BFGS:

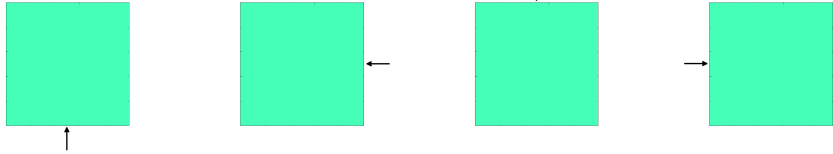
$$\mathbf{a}^{i+1}(\mathbf{x}) = \mathbf{a}^i(\mathbf{x}) - (B^i)^{-1} \nabla_a g[\mathbf{a}^i].$$

Fuentes láser pulsadas

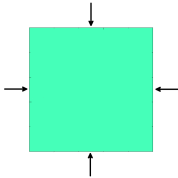


Los métodos MB y FMS

MB



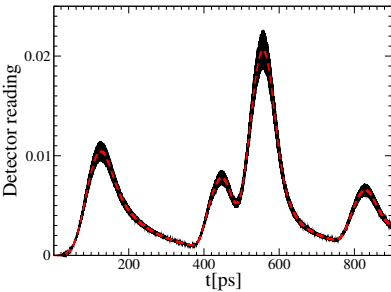
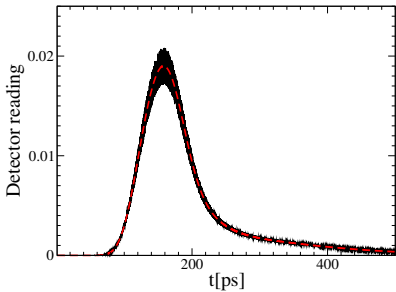
FMS



Los métodos MB y FMS

$$q = q_i(\mathbf{x}, \hat{\theta}, t) = \sum_{k=1}^{N_s} s_{k,i}(\mathbf{x}, \hat{\theta}, t), \quad i = 1, 2, \dots, N_q,$$

$$s_{k,i}(\mathbf{x}, \hat{\theta}, t) = \exp\left(-\frac{|\mathbf{x} - \mathbf{x}_{k,i}|^2}{2\sigma_x^2}\right) w\left(\frac{|\theta - \theta_{k,i}|}{\sigma_\theta}\right) w\left(\frac{|t - \tau_{k,i} - \sigma_t|}{\sigma_t}\right)$$



La función objetivo

Consideramos el operador de medición

$$G_j[u] = \oint_{\partial\Omega} \int_{\hat{\theta} \cdot \hat{\nu} > 0} [1 - f(\hat{\theta} \cdot \hat{\nu})] \hat{\theta} \cdot \hat{\nu} w\left(\frac{|\mathbf{x} - \mathbf{x}_j|}{\sigma_d}\right) u(\mathbf{x}, \hat{\theta}, t) d\theta dS.$$

Definimos la función objetivo

$$\Lambda[a] = \sum_{i=1}^{N_q} g_i[u_i],$$

con

$$g_i[u] = \frac{1}{2} \sum_{j=1}^{N_d} \int_0^T (G_j[u] - \tilde{G}_{j,i})^2 dt.$$

El método adjunto

Operador de transporte:

$$\mathcal{T}[u] \equiv \frac{1}{c} \frac{\partial u}{\partial t} + \hat{\theta} \cdot \nabla u + au + b \left[u - \int_{S^1} \eta(\hat{\theta} \cdot \hat{\theta}') u(\mathbf{x}, \hat{\theta}', t) d\theta' \right]$$

Para cada fuente generalizada q_i tenemos el problema de transporte

$$\mathcal{T}[u_i] = 0$$

$$u_i(\mathbf{x}, \hat{\theta}, t = 0) = 0$$

$$u_i(\mathbf{x}, \hat{\theta}, t) = f(\hat{\theta} \cdot \hat{\nu}) u(\mathbf{x}, \hat{\theta}_r, t) + q_i(\mathbf{x}, \hat{\theta}, t), (\mathbf{x}, \hat{\theta}) \in \Gamma_-$$

El método adjunto

Operador de transporte adjunto

$$\mathcal{T}^*[\lambda_i[a], a] \equiv -\frac{1}{c} \frac{\partial \lambda_i}{\partial t} - \hat{\theta} \cdot \nabla \lambda_i + (a+b) \lambda_i - b \int_{S^1} \eta(\hat{\theta} \cdot \hat{\theta}') \lambda_i d\theta' = 0.$$

y el problema de transporte *adjunto*

$$\mathcal{T}^*[\lambda_i[a], a] = 0$$

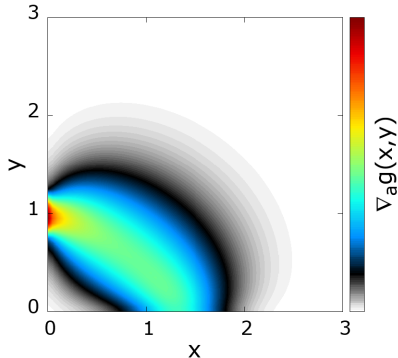
$$\lambda_i(\mathbf{x}, \hat{\theta}, t = T) = 0$$

$$\lambda_i(\mathbf{x}, \hat{\theta}, t) = f(\hat{\theta} \cdot \hat{\nu}) \lambda_i(\mathbf{x}, \hat{\theta}_r, t)$$

$$+ \sum_{j=1}^{N_d} \left(G_j[u_i] - \tilde{G}_{j,i} \right) \times [1 - f(\hat{\theta} \cdot \hat{\nu})] w\left(\frac{|\mathbf{x} - \mathbf{x}_j|}{\sigma_d}\right), (\mathbf{x}, \hat{\theta}) \in \Gamma_+.$$

El método adjunto

$$\nabla_a g_i(\mathbf{x}_{\ell_1, \ell_2}) = - \int_0^T \int_{\Omega} \int_{S^1} \lambda_i(\mathbf{x}, \hat{\theta}, t) \delta a(\mathbf{x}) u_i(\mathbf{x}, \hat{\theta}, t) d\theta d\mathbf{x} dt.$$



Fuente en $\mathbf{x}_s = (1.5, 0)$ cm y detector en $\mathbf{x}_d = (0, 1.0)$ cm.

Algoritmo de reconstrucción

Algoritmo 3 Pseudocódigo para la resolución del problema inverso

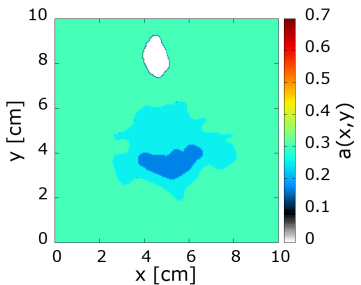
- 1: Dar una estimación inicial $a^0(\mathbf{x})$
 - 2: **para** $i = 1, \dots, i_{\max}$ **hacer**
 - 3: **para** cada fuente generalizada $q_j, j = 1, \dots, N_q$ **hacer**
 - 4: Resolver el problema directo por medio del Algoritmo 1
 - 5: Evaluar ec. (3.21), si $\Lambda[a] < C$ ir a 10.
 - 6: Resolver el problema adjunto mediante el Algoritmo 1
 - 7: **terminar**
 - 8: Construir el gradiente
 - 9: Llamar al algoritmo lm-BFGS para actualizar el coeficiente $a^{i+1}(\mathbf{x})$.
 - 10: **terminar** con $a(\mathbf{x}) = a^i(\mathbf{x})$
-

Reconstrucciones: modelo de cuello humano

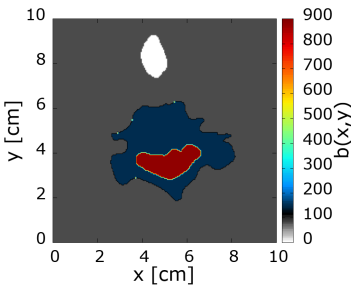


Reconstrucciones: modelo de cuello humano

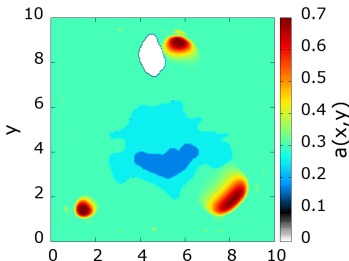
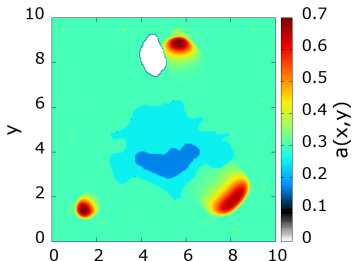
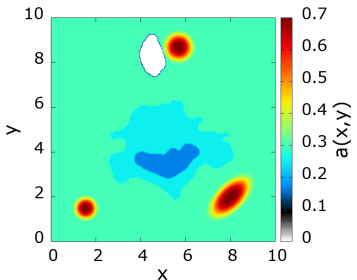
Coeficiente de absorción $a^0(x)$:



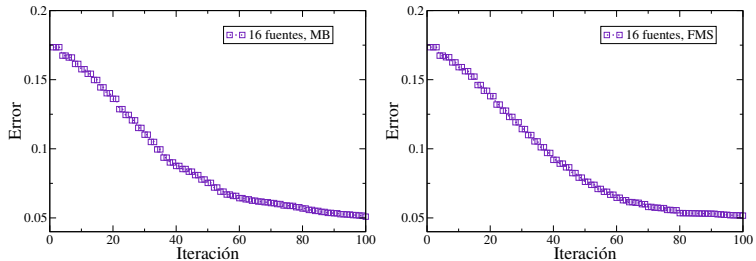
Coeficiente de dispersión $b(x)$:



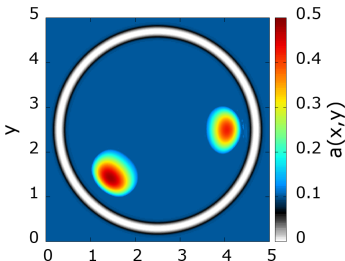
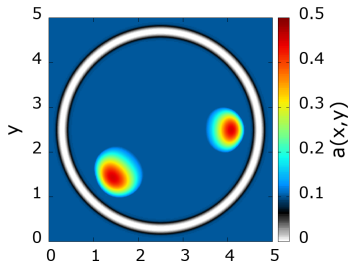
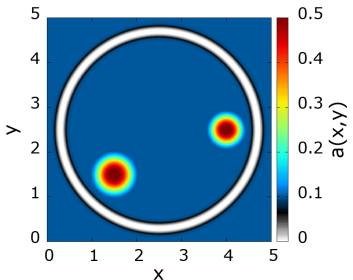
Reconstrucciones: modelo de cuello humano



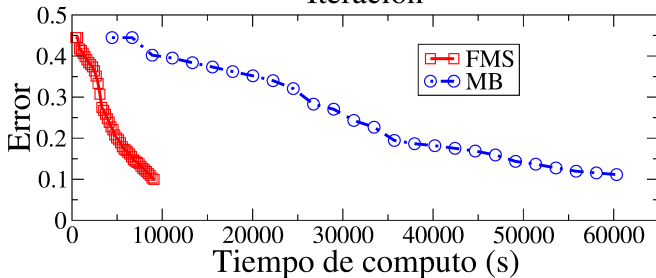
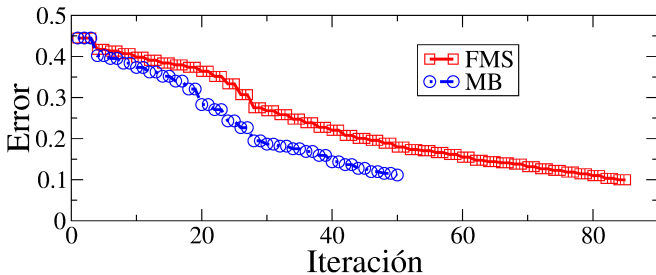
Reconstrucciones: modelo de cuello humano



Reconstrucciones: modelo de cabeza humana



Reconstrucciones: modelo de cabeza humana



Conclusiones

- ▶ Desarrollo de estrategias computacionales para el problema ETR.
- ▶ Validación con soluciones manufacturadas, analíticas y experimentos
- ▶ Caracterización de capas límite.
- ▶ Resolución de capas límite.
- ▶ Solución del problema inverso en TO.
- ▶ Tres estrategias principales:
 - Método FC-DOM de alto orden.
 - Paralelización con alta eficiencia.
 - Método FMS que acelera la reconstrucción.
- ▶ Se redujo el tiempo computacional requerido para la resolución del problema inverso en órdenes de magnitud.